

See discussions, stats, and author profiles for this publication at: <https://www.researchgate.net/publication/270817900>

Review on photonic crystal coatings for scintillators

Article in *International Journal of Modern Physics A* · November 2014

DOI: 10.1142/S0217751X14300701

CITATIONS

17

READS

353

2 authors:



Arno Knapitsch

Intel

28 PUBLICATIONS 681 CITATIONS

[SEE PROFILE](#)



Paul Lecoq

CERN

1,864 PUBLICATIONS 36,754 CITATIONS

[SEE PROFILE](#)

Some of the authors of this publication are also working on these related projects:



FOREST [View project](#)



EndoTOFPET-US [View project](#)

Review on photonic crystal coatings for scintillators

Arno Knapitsch* and Paul Lecoq[†]

*European Organization for Nuclear Research (CERN),
 1211 Geneva 23, Switzerland
 *arno.knapitsch@cern.ch
 †paul.lecoq@cern.ch*

Received 6 October 2014

Accepted 13 October 2014

Published 28 November 2014

The amount of light and its time distribution are key factors determining the performance of scintillators when used as radiation detectors. However most inorganic scintillators are made of heavy materials and suffer from a high index of refraction which limits light extraction efficiency. This increases the path length of the photons in the material with the consequence of higher absorption and tails in the time distribution of the extracted light. Photonic crystals are a relatively new way of conquering this light extraction problem. Basically they are a way to produce a smooth and controllable index matching between the scintillator and the output medium through the nanostructuration of a thin layer of optically transparent high index material deposited at the coupling face of the scintillator. Our review paper discusses the theory behind this approach as well as the simulation details. Furthermore the different lithography steps of the production of an actual photonic crystal sample will be explained. Measurement results of LSO scintillator pixels covered with a nanolithography machined photonic crystal surface are presented together with practical tips for the further development and improvement of this technique.

Keywords: Photonic crystals; light extraction; scintillators; RCWA; FDTD; Monte Carlo; light diffraction, nanolithography; nanoimprint.

PACS numbers: 42.79.Dj, 87.57.uk, 29.40.Mc, 78.67.Pt, 42.70.Qs, 85.40.Hp, 81.16.Nd

Contents

1. Introduction	2
1.1. Scintillator and scintillation basics	3
1.2. Increasing the light output	4
1.3. Optimizing the time distribution of extracted photons	5
1.4. Collimation of the extracted light	6
1.5. Related work	6
2. Photonic Crystal Basics	8
2.1. The reciprocal space and the Brillouin zone	8

2.2.	Band diagrams	10
2.3.	Light extraction with photonic crystal gratings	11
3.	Simulations	13
3.1.	Scintillator modeling using a Monte Carlo simulations tool	13
3.1.1.	Basic characteristics of SLITRANI	14
3.1.2.	Self-build extensions to SLITRANI	14
3.2.	Photonic crystal simulations	15
3.2.1.	MPB — MIT photonic bands	15
3.2.2.	CAMFR — CAvity Modeling FRamework	16
3.3.	Photonic crystals in combination with scintillators	17
3.4.	Light extraction efficiency calculations	17
3.4.1.	The influence of period and feature width	18
3.4.2.	Index of refraction and absorption	18
3.4.3.	Structure height	21
3.4.4.	Wavelength	21
4.	Sample Production and Results	21
4.1.	Results	24
4.1.1.	Light extraction gain	26
5.	Mass-Production Technologies	28
5.1.	Optical interference lithography	28
5.2.	Nanoimprint lithography	29
6.	Conclusion	29
	Acknowledgments	30
	References	30

1. Introduction

Inorganic scintillators are widely used as radiation detectors in a wide range of applications, such as high and medium energy physics and astrophysics detectors, spectroscopy, medical imaging, industrial nondestructive control systems, well oil logging, homeland security. For most of these detection systems the goal is to record the maximum of information about the event at the origin of the ionizing radiation, and in particular:

- its spatial localization,
- the precise determination of its energy,
- the time of the event.

The spatial localization is generally achieved by the combination of a number of individual detectors, finely segmented and distributed around the region of interest. The energy and timing resolution are on the other hand related to intrinsic properties of the detector itself. A good energy resolution is a prerequisite for spectroscopic measurements and requires a good linearity of the scintillator response as a function of the energy released in the detector as well as the highest possible light yield to not be dominated by photostatistics effects. There is an increasing demand in a number of applications for a very precise timing resolution. This is generally related to the study of ultra fast phenomena as well as to time-of-flight imaging techniques. A typical example is for high energy physics detectors at high luminosity colliders

for the association of the detected particle tracks to the correct vertex among the large quantity of events produced at each beam crossing. Another demand comes from medical imaging positron emission tomography, where it has been demonstrated that time-of-flight techniques can considerably improve the signal to noise ratio of the images with a direct impact on the reduction of the radioactive dose to be injected to the patient. Considering that it takes 3 ps for a photon to travel 1 mm in vacuum the requirement for an imaging system based on time-of-flight is extremely challenging. It can be shown that the timing resolution of a light emitting system is directly related to the timing density of the photons in the leading edge of the pulse.¹ The requirements for a good scintillator are therefore a high light yield and a short rise time and decay time. The energy resolution ΔE and the timing resolution Δt of the detectors are strongly influenced by the statistical fluctuations of the number of photoelectrons N_{pe} registered after a particle has deposited its energy in the scintillator. Typically, N_{pe} is expressed as:

$$N_{pe}[\text{pe/MeV}] = q_{\text{eff}} \cdot LY = q_{\text{eff}} \cdot \eta_L \cdot LY_{\text{abs}}, \quad (1)$$

where q_{eff} is the effective quantum efficiency of the photodetector, LY the number of scintillation photons arriving at the photocathode per MeV of absorbed radiation, and LY_{abs} the number of photons produced in the scintillator per MeV of absorbed radiation.

More commonly, LY and LY_{abs} are referred to as light output and absolute light yield of the scintillator, respectively. The parameter $\eta_L = LY/LY_{\text{abs}}$ is the light collection efficiency of the scintillation detector and summarizes the impact of all processes which lead to losses during the transport of the scintillation photons from the production point toward the active region of the photodetector. This includes absorption and scattering in the Crystal bulk, absorption and diffusion at enveloping materials, and reflection losses due to mismatch of the refractive indices of scintillator, optical coupling and photo detector. These losses increase the statistical fluctuations of the light output and therefore deteriorate ΔE and Δt . As a consequence the performance of the scintillator can be severely affected by the transit of the photons from the interaction point to the photodetector where they will be converted into an electronic signal, leading to delays and absorption losses. To enhance the photon coupling between detector and scintillator we have proposed already several years ago to use a thin photonic crystal (PhC) slab to diffract light outside the extraction cone.²

1.1. Scintillator and scintillation basics

Scintillators are among the most popular ionizing radiation detectors. For many applications the density and hence the compactness of the detector is essential in order to reduce the detector volume and cost. This is achieved by using high stopping power and therefore high density materials. It allows a reduction of the shower size of high energy γ -rays and electrons as well as the range of Compton scattered photons for lower energy γ -rays. A dense material will also reduce the

lateral spread of the shower, which is particularly important for the majority of high energy physics detectors. Inorganic scintillators are wide bandgap ionic materials and high density implies the choice of anions and cations of high atomic number A (and therefore high Z), as well as small ionic radius to increase the ionic density in the crystal lattice. From this point of view oxides are generally denser than iodides because of the much smaller ionic radius of the oxygen as compared to the iodine ion, in spite of its lighter weight. Similarly the oxidation potential of the anion is important as it allows reducing the number of anions (generally light) needed to compensate for the positive charge of the much heavier cation. For this reason oxygen is a better ligand than the slightly heavier fluorine ion because of its higher oxidation state (2 or 3 instead of 1). As a result inorganic scintillators are materials with a high electronic density, which generally implies a high refractive index. As an example of commonly used high density crystals are Bismuth Germanate (BGO: 7.13 g/cm^3 , $n = 2.15$) or Lutetium Orthosilicate (LSO: 7.40 g/cm^3 , $n = 1.82$). Crystals with a density higher than 8 g/cm^3 are currently available, such as Lead Tungstate (PWO: 8.28 g/cm^3 , $n = 2.2$) or Lutetium Aluminum Perovskite (LuAP: 8.34 g/cm^3 , $n = 1.94$). Materials of even higher density in the range of 10 g/cm^3 are being identified and studied, such as: Lutetium Oxide: Lu_2O_3 , Lutetium Hafnate: $\text{Lu}_4\text{Hf}_3\text{O}_{12}$, Lutetium Tantalate: Lu_3TaO_7 , Lutetium Lead Tantalate: $\text{LuPb}_2\text{TaO}_6$, Thorium Oxide: ThO_2 .

1.2. Increasing the light output

Each interaction of an ionizing particle with the medium leads to the excitation of the atoms in a volume small compared to the crystal dimensions, i.e. a sphere of $100 \mu\text{m}$ radius. As a result from the atomic de-excitation scintillation photons are emitted isotropically. Therefore each photon can be emitted with an angle θ_1 from the x -axis and θ_2 from the y -axis. Figure 1 illustrates this process in two dimensions for a gamma interaction point in the middle of a rectangular and unwrapped LSO crystal pixel. According to Snell's law this angle determines if each photon can reach the photodetector or not. We can consider two cases: either the crystal is in dry contact with the photodetector (i.e. dry coupling) or we use a coupling grease or glue with a typical index of refraction of 1.41 (see Fig. 1).

From Fig. 1 one can distinguish four main propagation modes. Their different properties and extraction probabilities can be seen in Table 1.

It can be seen that the number of direct photons is less than 20% for glue coupling. More than half of the photons are escaping the crystal through the lateral faces. A fraction of them can be recuperated by the use of coating or wrapping materials. But these photons will be more delayed as compared to the direct photons and will suffer absorption losses due to a longer travel path in the bulk. And still, they have to fall into the light extraction cone to get extracted, otherwise they are back reflected and even more delayed. The potential of PhCs now is to increase this light extraction cone which will allow an increasing number of photons to escape the crystal.

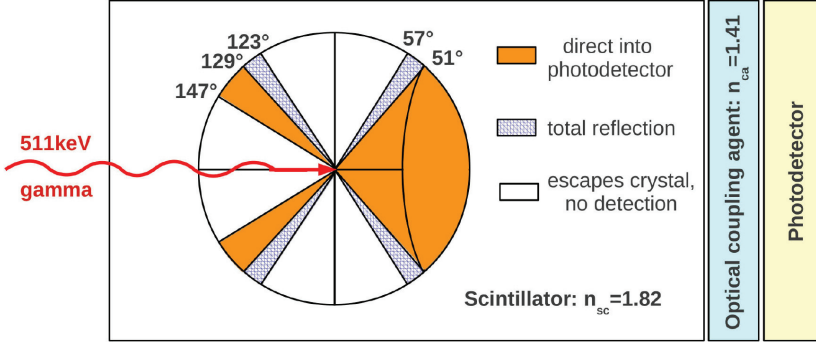


Fig. 1. Two-dimensional (2D) representation of the different photon propagation modes in a LYSO crystal covered by a layer of Silicon grease on the coupling face to the photodetector.³

Table 1. Angular modes of scintillation photons in a rectangular LSO crystal (index 1.82) in the case of glue coupling (index 1.41) toward the photodetector.

Emission range θ	Description	% of photons
$0^\circ < \theta < \arcsin(1.41/1.82) = 51^\circ$	Photons couple directly to the photodetector	18.5
$51^\circ < \theta < 90^\circ - \arcsin(1/1.82) = 57^\circ$	Total internal reflection, photons cannot escape	4.2
$57^\circ < \theta < 90^\circ + \arcsin(1/1.82) = 123^\circ$	Photons escape laterally into air	54.6
$123^\circ < \theta < 180^\circ - \arcsin(1.41/1.82) = 129^\circ$	Total internal reflection, photons cannot escape	4.2
$129^\circ < \theta < 180^\circ - \arcsin(1/1.82) = 147^\circ$	Photons in total internal reflection, photons can be detected after back reflection	10.4
$147^\circ < \theta < 180^\circ$	Photons lost on the back face	8.1

1.3. Optimizing the time distribution of extracted photons

In a simplified setup, considering no wrapping and no diffusion and a glue coupling to the detector, the formulation of the travel path difference between a direct photon emitted in direction of the photodetector ($t_{\text{direct}} = 0$) and the most delayed photon (traveling back and forth in a total reflection mode) is given by the following formula:

$$t_{\text{max_photons}} = \frac{2L}{c} n_{\text{sc}} \left(\frac{1}{\cos \left(\arcsin \frac{n_{\text{gr}}}{n_{\text{sc}}} \right)} \right) \quad (2)$$

with n_{sc} being the refractive index of the LSO crystal and n_{gr} that of the silicon grease. This formula is derived from the maximum travel path a photon can take in such a setup. In particular, such a photon would be emitted in the backward direction and at an angle that allows it to be totally reflected by the side and back

walls so that it can come back to the detector (e.g. see $\theta = 129^\circ$ in Fig. 1). The path length of such a back and forth reflected photon would be the hypotenuses of a right triangle where the length of the adjacent side is two times the crystal length. This relation holds independent from the crystal diameter and is also valid in the three-dimensional (3D) case. Assuming a uniform distribution of this photon transit time, the contribution $\text{FWHM}_{\text{photons}}$ to the time resolution due to the transit of the photons emitted in the center of a 20 mm long LSO crystal is:

$$\text{FWHM}_{\text{photons}} = \frac{4.7L}{c} \sqrt{\frac{1}{12}} n_{\text{sc}} \left(\frac{1}{\cos \left(\arcsin \frac{n_{\text{gr}}}{n_{\text{sc}}} \right)} \right) \quad (3)$$

keeping in mind that $\text{FWHM}_{\text{photons}} = 2.35\sigma_{\text{photons}}$ and that the σ_{photons} of a uniform distribution is defined as $\sqrt{1/12} * t_{\text{max_photons}}$. This calculation shows nicely the different factors influencing the photon travel path and their contribution to the time resolution. In a real setup photons can be back reflected several times before they get extracted, each time adding several hundreds of ps to the travel time. By increasing the light extraction efficiency at the outcoupling face, PhCs will reduce the multiple bouncing effects and improve therefore the time resolution of scintillator-based detectors in two ways:

- (1) By a compression of the time distribution of the light propagation modes: the population of the first hit extracted photons will increase and the tail in the time distribution of extracted photons due to multiple bouncing will be reduced.
- (2) By a decrease of the overall photon travel path of the photons, which will reduce the absorption losses and contribute to a better photo-statistics.

1.4. Collimation of the extracted light

If properly designed PhCs can shape the light distribution in addition to the improvement in light extraction efficiency. This effect can be useful if one wants to collimate the light from a scintillator onto a photodetector which could potentially increase the detection efficiency by avoiding grazing angles. In recent work we have demonstrated this effect on a LSO crystal which was covered with a PhC grating. These measurements can be seen in Fig. 2 where the angular distribution (AD) of the light output of these two PhCs is compared to the light AD of a reference crystal, which has remained untreated. The results confirm that both PhC patterns (P2 and P6) increase the light output, but also that P2 has in additional collimation effect in the forward direction.

1.5. Related work

Almost three decades ago, PhC structures have been suggested the first time for light extraction enhancement in light emitting diodes.^{4,5} The first actual version of a PhC though was consisting of a face centered cubic (FCC) arrangement of 6 mm spheres of a dielectric material which of course only had a band gap for

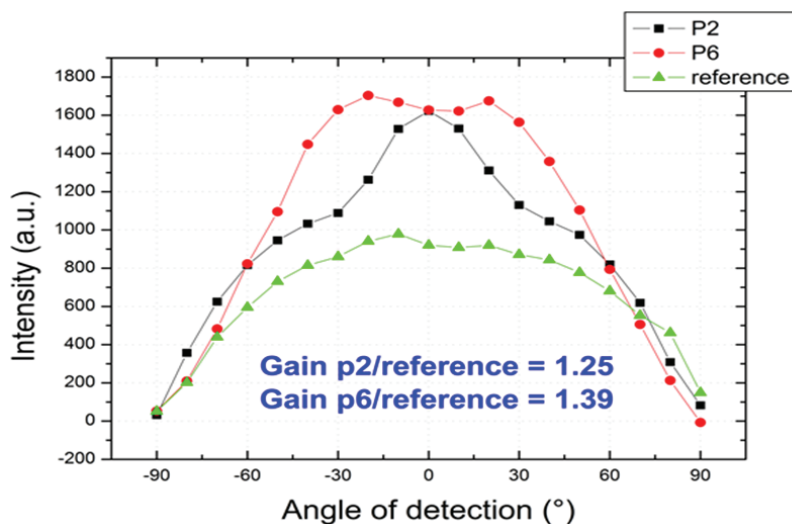


Fig. 2. Angular distribution of extracted photons from two PhCs deposited on a LSO crystal (P2 and P6) as compared to the flat LSO reference. On top of the improved light extraction efficiency P2 shows a strong collimation effect in the forward direction.

microwaves.⁶ This idea was based on a 3D photonic band gap (PBG) which was difficult to produce in a nanoscale at that time so that a few years passed until the first full 3D PBG was demonstrated for visible wavelengths. Later on, different 2D PhC structures were suggested to enhance light extraction of PhCs, some of them were aimed to enhance spontaneous emission by forbidding certain guided modes in these structures.⁷ In other cases the 2D PhC structures were operated mostly outside the PBG wavelength acting as a diffraction grating.^{8,9} In 2008 Kronberger *et al.* theoretically investigated the concept of PhC gratings on heavy inorganic scintillators (HISs).² In that work, a PhC grating was designed to enhance the light coupling efficiency between the scintillator and a photo detector and a theoretical gain could be shown. In the following work of Knapitsch *et al.* first nanolithography results were shown on top of scintillating crystals.¹⁰ Following these investigations, they could produce several LSO scintillator pixels fully covered with a silicon nitrate PhC grating at the out-coupling crystal face.^{11,12} The samples in that work could show significant light extraction gain over a conventional scintillator pixel when coupled without optical glue to a photodetector. Meanwhile, Pignalosa *et al.* used silicon nitrate nanocones in order to enhance the performance of a LSO scintillator film used in medical X-ray detectors.¹³ In the work of Zhu *et al.* a 2D PhC array made by polystyrene nanospheres is used to enhance the light output of a Tb³⁺ doped glass scintillator.¹⁴ In 2014 the same group published a paper about applying a similar nanosphere light extraction technique on top of a BGO scintillator.¹⁵ A nonphotonic, but similar micro-surface structuring approach is described in the work of Cates *et al.* in 2013.¹⁶ There, laser etching is used to generate a quasiperiodic

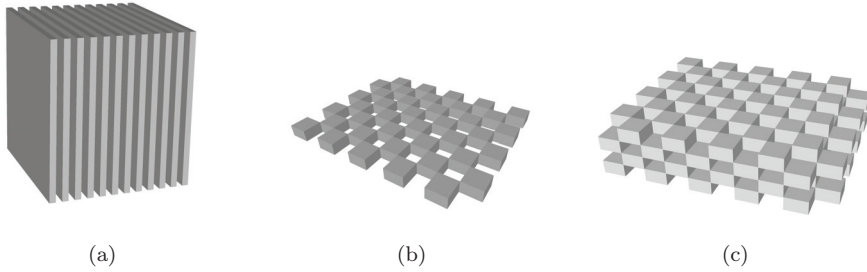


Fig. 3. The different dimensional arrangements of PhCs. Photonic crystals are composed of a periodic dielectric or metallo-dielectric that affects the propagation of electromagnetic waves in one, two or three dimensions.

micro-pattern on top of a YAP:Ce scintillator. Without optical coupling agents, which could not be used due to the high operation temperature, the laser etched pattern showed a light extraction improvement of 90%.

2. Photonic Crystal Basics

Photonic crystals are natural or artificial materials which have a periodic arrangement of different dielectric materials in one, two, or three dimensions (see Fig. 3). The spatial arrangement hereby is in the range of the wavelength of the photons. While PhC can be found in nature in various forms (e.g. opals or butterfly wings¹⁷) the first time PhCs were described in literature in 1987 by Eli Yablonovitch and Sajeev John.^{4,5} Their intention was to develop a material showing similar effects on photons as semiconductors to electrons. Many applications were arising from this basic idea but the principle of PhCs is always the same: light is scattered at the interfaces where the index of refraction changes and the scattered waves can now interfere constructively or destructively with each other. The stationary properties of the light that are allowed to travel are called modes. While the modes of propagation in a homogeneous medium are plane waves, the modes of a periodic medium are known as Bloch modes. A Bloch mode can be seen as a standing wave field produced by the multiple coherent scatterings of a wave by the periodic structures of a PhC lattice.

2.1. The reciprocal space and the Brillouin zone

In solid state physics, a lattice is often represented as a reciprocal lattice (RL), which is the Fourier transform of the spatial function of the original lattice. The Brillouin zone (BZ) is a primitive cell in reciprocal space where the boundaries are defined by planes related to points on the RL (see Figs. 4 and 5). The high symmetry points within the BZ are labeled according to Table 2. The RL vectors of the two PhC patterns used in this work can be calculated according to the formulas shown in Table 3. In photonics, but also in solid state physics, the BZ description is important since a periodic structure can be completely characterized by just looking into the solutions of the first BZ. Wave vectors outside the BZ are folded by the edges of the BZ and can be therefore represented by a wave vector inside the BZ again.

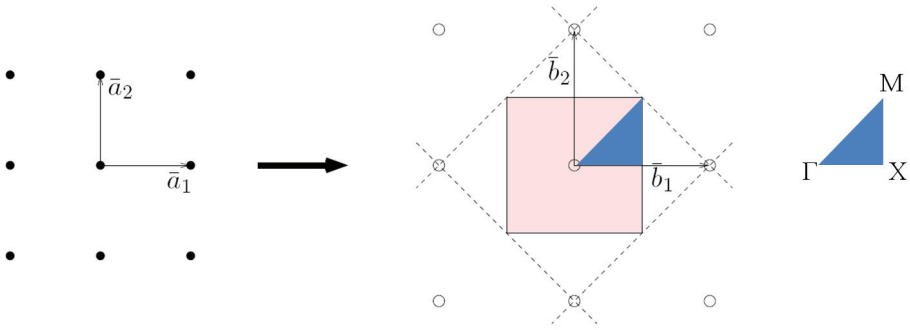


Fig. 4. (Color online) Square lattice and corresponding RL with highlighted BZ (red). The blue area is the irreducible first BZ with the corners M , K and X .

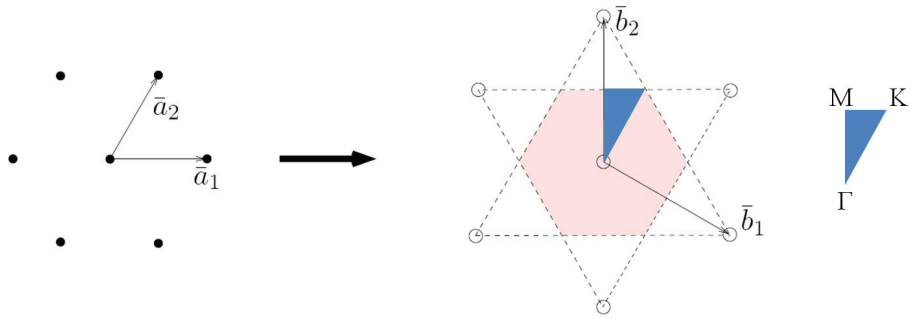


Fig. 5. (Color online) Triangular lattice and corresponding RL with highlighted BZ (red). The blue area is the irreducible first BZ with the corners M , K and Γ .

Table 2. Critical points of the first BZ of a RL, which are points of high symmetry and are therefore of special interest in photonics and solid state physics.¹⁸

Symbol	Description
Γ	Center of the BZ
M	Center of an edge
X	Center of a face
K	Middle of an edge joining two rectangular faces

Table 3. Transformation of the RL vectors for two-dimensional square and triangular patterns. \hat{x} and \hat{y} are the independent lattice vectors and a is the lattice constant.

	Real lattice	Reciprocal lattice	RL length
Square lattice	$\mathbf{a}_1 = a\hat{x}$ $\mathbf{a}_2 = a\hat{y}$	$\mathbf{b}_1 = (2\pi/a)\hat{x}$ $\mathbf{b}_2 = (2\pi/a)\hat{y}$	$2\pi/a$
Triangular lattice	$\mathbf{a}_1 = a\hat{x}$ $\mathbf{a}_2 = (\hat{x} + \sqrt{3}\hat{y})$	$\mathbf{b}_1 = (2\pi/a)(\hat{x} - \sqrt{3}/3\hat{y})$ $\mathbf{b}_2 = (4\pi/a)(\sqrt{3}/3)\hat{y}$	$4\pi/(a\sqrt{3})$

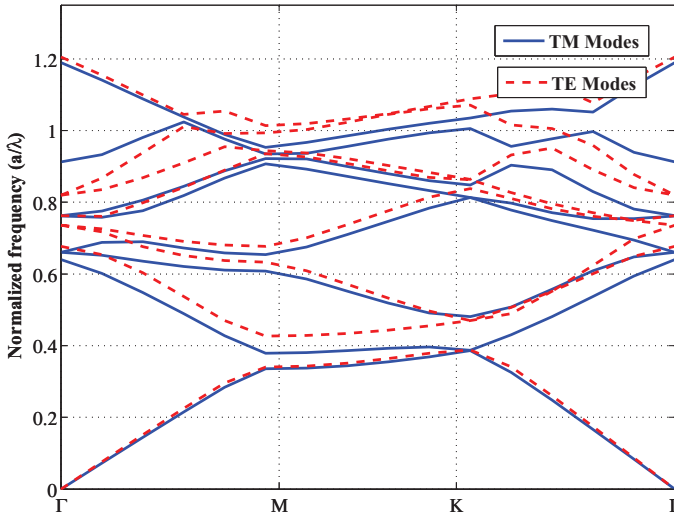


Fig. 6. Band diagram of a 2D triangular PhC with a hole diameter of $0.3a$ and an index of refraction of the substrate of 1.85 (silicon nitride). The bands are calculated with the help of the MIT Photonic-Bands (MPB) package.¹⁹

2.2. Band diagrams

The discrete eigenvalues $\omega_n(\mathbf{k})$ indicated by $n = 1, 2, 3, \dots$ are continuous functions of \mathbf{k} . When $\omega_n(\mathbf{k})$ is plotted versus the wave vector \mathbf{k} we get the band or dispersion diagram of the PhC structure. Therefore the band diagram relates the corresponding photon energies $\omega(\mathbf{k})$ of each mode to the corresponding propagation direction \mathbf{k} . For a 2D PhC with triangular holes of air in silicon nitride (IR = 1.85) with infinite extension in the z -direction the band diagram looks like shown in Fig. 6. The PhC pattern structure used in this plot can be seen in Fig. 5. The hole diameter was chosen to be $0.3a$ and the index of refraction of the substrate is 1.85 (e.g. silicon nitride). The fields in a 2D PhC structure can be divided into two polarizations: transverse magnetic (TM) and transverse electric (TE). In the TM mode the magnetic field is perpendicular to the plane of incidence (plane which contains the surface normal and the propagation vector) and in the TE mode the electric field is perpendicular to the plane of incidence. In reality, the thickness of the PhC structure is limited. PhC structures with finite thickness are called PhC slabs or planar PhCs. The finite thickness introduces different behaviors to the PhC and therefore a PhC slab cannot be treated as a purely 2D PhC. If we take the example of Fig. 6 and limit the thickness to $1.6a$ the modes look different (see Fig. 7). In this plot, the modes are categorized in even and odd modes instead of TE and TM modes. The reason for that is that modes are not completely parallel or vertical when going away from the $z = 0$ plane. But due to the continuity of fields, even modes are mostly TE and odd modes are mostly TM and are therefore also called TE-like and TM-like modes respectively.²⁰

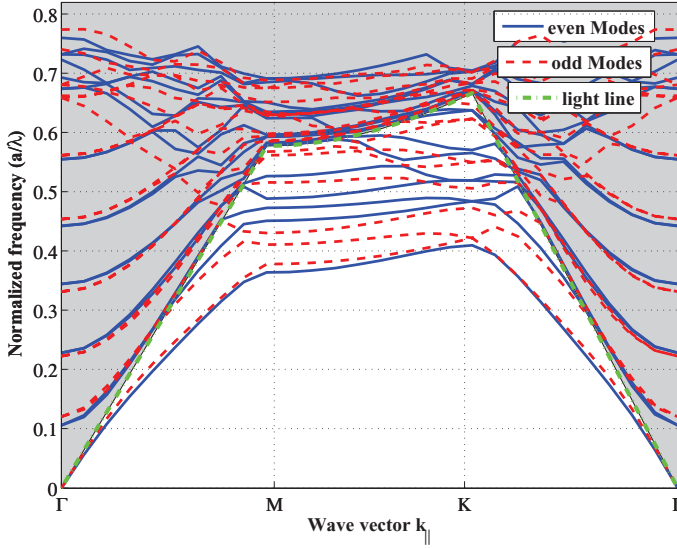


Fig. 7. (Color online) Band diagram of a triangular PhC slab with a hole diameter of $0.3a$, a thickness of $1.6a$ and an index of refraction of the substrate of 1.85 (silicon nitride). The 18 bands are calculated with the MPB software package.¹⁹ The PhC pattern in this plot has a lattice constant of $a = 280$ nm which results in a normalized frequency of 0.66 at an emission wavelength of 420 nm. It can be seen, that a large fraction of the modes are placed above the light line which means that they can radiate into the ambient air.

The green dash-dotted line in Fig. 7 represents the light line. The light line indicates the border to the light cone ($\omega \geq ck_{||}$), the region where modes can irradiate into air. In air (or vacuum) this relation is simply $\omega(k) = k_0c$. Modes in that region are also called leaky since they “leak” into the ambient medium. The band diagrams in this work are calculated using the freely available MPB tool which is a software package released under the GPL (GNU General Public) license. The MPB software calculates eigenstates and eigenvalues of the Maxwell equations in the frequency domain. For that it applies a Fourier transform over an infinite repetition of the unit cell (smallest entity of the PhC pattern) in all three directions to avoid discontinuities. For 3D problems like the PhC slab we are using, this can introduce some problems since the unit cell is not repeated in the z -direction. For PhC slabs, MPB can therefore only calculate the guided modes (below the light line) with high accuracy. As a solution, the unit cell size is extended into the z -direction by several lattice constants (3 to 8 times the lattice constant a) which reduces the influence of the z -periodicity on the leaky modes to a negligible amount.²¹

2.3. Light extraction with photonic crystal gratings

When describing the incident light with the wave vector k_i having the length $|k_i| = n_i k_0$ where k_0 is the vacuum vector length $k_0 = 2\pi/\lambda_0$, Snell’s law is equivalent to the conservation of the length of the in-plane vector $k_{||}$ which is the vacuum vector

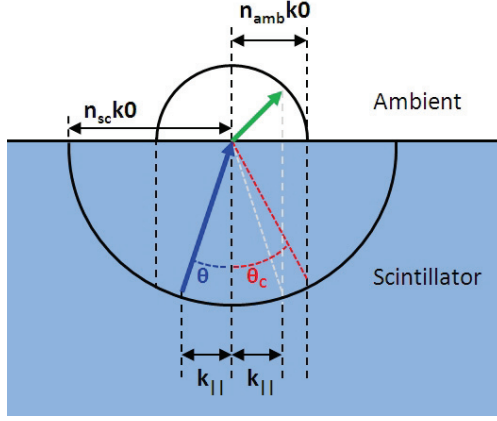


Fig. 8. K -vector diagram of a scintillator/ambient interface. Due to Snell's law, light can only escape the crystal when the angle is smaller than the critical angle $\Theta < \Theta_c$. Snell's law can also be derived from the conservation of the in-plane vector k_{\parallel} which is the k -vector component parallel to the interface. The vacuum vector length is $K_0 = 2\pi/\lambda_0$ which does not change in the case of air. In the diagram we can see that for light in the ambient medium k_{\parallel} cannot get bigger than $n_{\text{amb}}k_0$ and therefore light having a bigger angle than Θ_c will be internally reflected.

multiplied by the index of refraction of the regarding material: $|k_{\parallel}| = nk_0$. Therefore only light with an in-plane k vector length smaller than $k_0 n_{\text{cry}} \sin \Theta_c = n_{\text{amb}}k_0$ can radiate into the ambient medium (see Fig. 8).

To overcome this limit, a theoretical investigation of PhC structures as diffraction gratings on top of scintillators was started in the work of Kronberger *et al.* and Knapitsch *et al.*^{2,10,22} PhCs are a periodic arrangement of two different materials in one, two or three dimensions. Currently, 2D PhC structures are used for the light yield improvement on HISs. In this work, the PhC slab on top of our scintillator operates as a diffraction grating. That means, that the PhC "Bragg scatters" the light out of the scintillator, leading to higher extraction efficiencies.²³ A 2D PhC structure can be described by its RL vectors G_i . The RL vector G can be derived by Fourier transformation of the real lattice (see Fig. 9) where the length of it is defined as $G_0 = 2\pi/a$ for a triangular pattern. These vectors couple light wave propagation in the PhC and the resulting mode is called a Bloch mode which is a linear combination of in-plane harmonic waves.²⁴ The diffraction condition to air is then described as $|k_{\parallel} + nG| < k_0$. The main harmonic (k_{\parallel}) couples to other harmonics by the RL vector G , if the resulting vector ($k_{\parallel} + nG$) lies within the air circle (radius = k_0), the mode propagates into air and is called leaky (see Fig. 10).²⁵ The integer n determines which harmonic is responsible for the diffraction. Looking at these modes in a dispersion diagram (also called band diagram), light diffraction can be explained as modes which exist above the light line.²⁶ A dispersion diagram relates the photon energies $\omega(k)$ to the corresponding propagation direction k . In air (or vacuum) this relation is simply $\omega(k) = k_0c$ which is called the light line when plotted in the dispersion diagram (see Fig. 7).

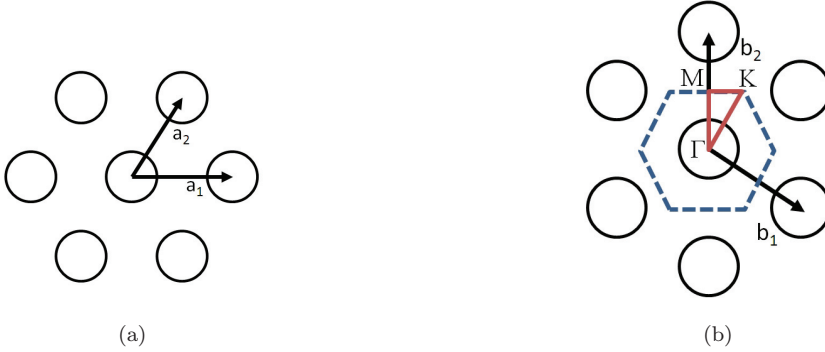


Fig. 9. (Color online) The real lattice (a) of the triangular PhC pattern with the lattice vectors a_1 and a_2 which vector length is the lattice constant a . In (b) the RL of the same structure can be seen. The length of b_1 and b_2 can be calculated as: $|b| = 2\pi/a$. The dashed hexagon represents the BZ and the red triangle the irreducible BZ.

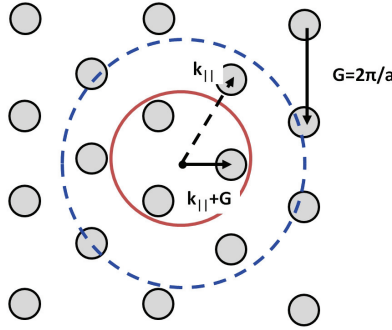


Fig. 10. (Color online) Ewald construction for a Bloch mode diffracted in the PhC slab. Light within the crystal having an in-plane wave vector k_{\parallel} (dashed pointer) cannot couple to the ambient air because its in-plane k -vector lies outside the air circle (red solid circle, radius $= n_{\text{air}}k_0$). Due to the presence of the periodic grating, the light can couple along the RL points to other harmonics (solid pointer). If the resulting vector lies within the air circle, the mode radiates into air (compare diffraction condition to air: $|k_{\parallel} + nG| < k_0$).

3. Simulations

Two different software packages had to be used for the simulations of a scintillator crystal detector setup which contains a PhC grating. At the present time, there is no proper tool known which could solve the problem of 3D light ray tracing when photonic elements are present. Therefore the problems were separated and special functions and methods were developed to combine the results.

3.1. Scintillator modeling using a Monte Carlo simulations tool

Monte Carlo computer simulations are named after the gambling city Monte Carlo because they are calculations based on random numbers, similar to games of chance. The interactions of radiation with matter occur randomly but the interactions occur

with known probabilities. A computer simulation which takes these probabilities into account can simulate individual radiation events and also the excitation, light emission and light propagation of a scintillator. A simulation with a large number of events can give a precise prediction of the parameters of the modeled system. In this work the LITRANI Monte Carlo computer simulations are used to study the light yield and AD of HISs and the effects of wrapping and optical contact materials. In addition it is used for the model matching technique to discriminate parameters of the crystal which cannot be measured otherwise.

3.1.1. *Basic characteristics of SLITRANI*

SLITRANI is a Monte Carlo program based on ROOT.^{27,28} In this work the newest version of LITRANI was used called SLITRANI which stands for “Super Light TRansmission in ANIsotropic media.” Any 3D setup which can be described by the TGeo class of ROOT can be used as a setup in SLITRANI. Each volume can be of a different material and each material can have a different dielectric constant, absorption length and diffusion length which may be dependent on the wavelength. In addition, wavelength shifting and Rayleigh scattering can be simulated. In contrast to other Monte Carlo light ray tracing programs, LITRANI can use an anisotropic dielectric constant and absorption length. To produce photons in SLITRANI one has various possibilities: spontaneous emission of photons, photons coming from an optical fiber, photons generated by ionizing particles, photons generated by gamma rays of energy of 0.1–1 MeV or photons generated by a high energy electromagnetic shower. As detectors one can have any volume and material inside the setup. In general all photons are tracked until they are absorbed or detected. In addition several photon statistics are recorded like the amount, arrival time, wavelength and material of absorption or reflection.

3.1.2. *Self-build extensions to SLITRANI*

Several functions and lines of code were added to make the standard SLITRANI version suitable for our purpose. Most of these added functions do not concern or change the physics of the program and are mostly about storing additional photon statistics along the track of a photon.

Angular distribution. The standard version of SLITRANI does not record the angle of the photon at each interface. Since the AD is of special interest for our purpose, we changed the source code in a way to keep track of the angle incoming and outgoing of an interface of interest. Since we assume random polarization we just store the angle between the normal vector of the surface and the traveling path of the photon.

Full access to photon statistics. For a better understanding of all the factors influencing the light distribution, reflection, absorption and light output, we introduced a variable into the source code which stores the information of birthplace,

initial emission angle, number of reflections from the wrapping and number of reflections at the out-coupling interface. The variable can be accessed after the simulation for analysis, plotting or debugging.

Additional light extraction due to rough surfaces. LITRANI can model an arbitrary combination of specular and diffuse reflection at any interface of two different materials. In the case of rough surfaces, diffusion may not always be a sufficient model to describe the light propagation correctly. The not perfectly flat surfaces of a scintillator can show some additional diffraction effects resulting from random phase variations induced by reflections from micro-topographic surface features.^{29–31} In the self-built LITRANI extension, an additional parameter can be chosen for each interface to enable additional light extraction of rough surfaces.

3.2. Photonic crystal simulations

The simulation of PhC structures in one, two, or three dimensions is a complex and nontrivial problem. Numerous mathematical techniques were developed during the last decades. Many commercially and freely available software packages exist. They can be used to simulate photonic bands, scattering matrices, field patterns, light extraction efficiencies, reflection and transmission coefficients or resonant cavities of PhCs. Their applicability depends mainly on the exact application and every technique has its advantages and disadvantages. A good overview of the different computational methods and modeling tools can be seen in Ref. 32. In our work only two different software packages were used to calculate the PhC properties of the extraction gratings. To calculate the photonic bands of a PhC slab in Fig. 7 the MIT MPB package has been used.¹⁹ For the calculation of field patterns and extraction efficiencies the CMFR package has been used.³³ The principles of these two simulation tools are summarized in the following sections.

3.2.1. MPB — MIT photonic bands

The freely available MPB tool is a software package released under the GPL (GNU General Public) license. MPB uses a fully-vectorized, 3D algorithm to compute the definite-frequency eigenstates of Maxwell's equations in arbitrary periodic dielectric structures. The number of eigenstates and band numbers can be chosen by the user. The algorithm applies a Fourier transform over an infinite repetition of the unit cell (smallest entity of the PhC pattern) in all three dimensions. The disadvantage of that method is, that for 3D problems like the PhC slab we are using, this can introduce some problems since the unit cell is not repeated in the z -direction. For PhC slabs, MPB can therefore only calculate the guided modes (below the light line) with high accuracy. As a solution, the unit cell size is extended into the z -direction by several lattice constants (3 to $8a$), which reduces the influence of the z -periodicity on the leaky modes to a negligible amount.²¹

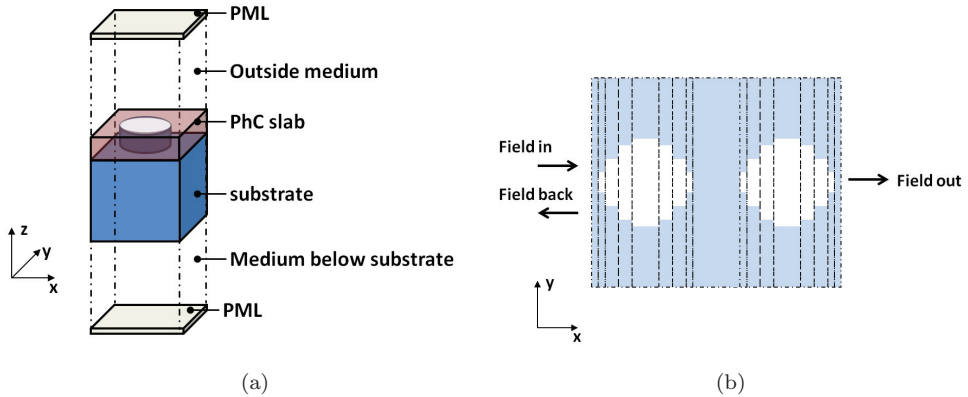


Fig. 11. (a) Computational unit cell enclosed by perfectly matched layers in z -direction and infinitely periodically repeated in the x - and y -directions. (b) Fourier expansion of the PhC structure in the xy -plane.

3.2.2. CAMFR — CAvity Modeling FRamework

For the simulation of the PhC structures a Rigorous Coupled Wave Analysis (RCWA) algorithm implemented in the CAvity Modeling FRamework (CAMFR) software package was used.³³ CAMFR is a common tool for the electromagnetic study of nanoscaled gratings in multilayer structures. The software is based on an eigenmode expansion algorithm and works for one- or two-dimensional PhC gratings. The RCWA algorithm uses a unit cell which can have any arbitrary geometry. An example of a unit cell can be seen in Fig. 11. In the RCWA method, special boundary conditions have to be applied in directions where the unit cell is not repeated periodically. For that reason, usually the perfect matching layer (PML) approach is used. A PML represents a nonphysical material that absorbs waves without any reflection, at all frequencies and angles of incidence.³⁴ The sides of the computation unit cell where no PML is applied are assumed to be periodically repeated in the corresponding directions. The PhC layer in the RWCA method is implemented as a Fourier expansion of slices of different index of refractions in the xy -plane (see Fig. 11(b)). The accuracy of the method increases with the number of slices. As a disadvantage, the computational effort increases as well and therefore it is recommended to keep the number of slices to a reasonable amount. The input and output fields of the whole structure are computed by matching the boundary conditions and are then computed by the scattering matrix technique.³⁵

In CAMFR, a unit cell is divided into slices perpendicular to the direction of propagation. In each slice, the refractive index is constant in the propagation direction. The different sections are then joined with the scattering matrix technique to model nonuniformity in propagation direction.³⁵

3.3. Photonic crystals in combination with scintillators

We do not know any light ray tracing software which also can simulate PhCs, therefore these two parts have been treated separately. The PhC slab has been simulated with the PhC simulation toolkit named CAMFR. The optical transition and reflection properties were calculated using this software and then integrated as a look-up table into the source of the Monte Carlo program LITRANI.²⁷ LITRANI was used to study the light propagation within a HIS setup. It traces photons throughout any combination of 3D shapes with different optical properties. The photons can be generated by different types of sources and will be tracked from their birth until absorption or detection. In our case, the emission light was produced using 662 keV photons from a point source (Caesium-137) at a distance of 1 cm. The photo absorption coefficients were taken from the NIST database,^a the index of refraction, attenuation and diffusion coefficients of the crystal were taken from laboratory measurements. The PhC diffraction effect depends on the angle of the photon impinging on the PhC and on the number of times they reappear when they get reflected. In particular the reflection property of a PhC slab varies with the inclination angle Θ (angle between the photon direction and the normal of the interface at the impinging point), the azimuth angle ϕ and polarization (TE or TM) of the photon. Our simulation has shown the strongest dependency on the inclination angle Θ , therefore we have been averaging the photons over all polarizations and azimuth angles to give us a simplified model where the distribution as well as the reflectance is only a function of Θ .

3.4. Light extraction efficiency calculations

In the following section the influence of different PhC pattern parameters to the light extraction capability is discussed and shown by means of CAMFR simulation results. To better show the PhC effect, the efficiency calculations assume an isotropic emitter inside the bulk material rather than the input function one would get with a scintillator pixel. Therefore the plots here show the transmission one would get for a given impinging angle. To see what effect the PhC structure would have on an actual scintillator the AD of the impinging photons on the extraction side of a scintillator has to be weighted by these transmission plots.

There are a number of variables which can change the light diffraction properties of PhC gratings. The most important parameters are summarized in Table 4. In the following figures, the influence of these parameters on the light extraction efficiency of PhCs are shown. If not stated otherwise, all the PhC design parameters are assumed to have the values of the optimal design considering realistically producible materials and dimensions (see Table 4). The x - y and x - z cross-section of such a structure and the index of refraction of it can be seen in Fig. 12.

^aNIST XCOM: Photon Cross Sections Database.

Table 4. Different parameters of a simple PhC diffraction pattern consisting of triangular placed poles of a high index of refraction material. The range of the dimensions is an approximation especially for our application of PhCs on scintillators and cannot be applied generally.

Symbol	Description	Usual dimensions	Optimized for a LYSO pixel
h	Height of the structure	0–800 nm	300 nm
L	Period of the features	300–800 nm	650 nm
D	Diameter of the features (% of L)	10–95%	455 nm
IR	Real part of the index of refraction of the PhC material	1.8–2.5	2.5
IR_k	imaginary part of the index of refraction of the PhC material (absorption)	0–0.01	0
λ	Wavelength of the plane wave	380–460 nm	420 nm

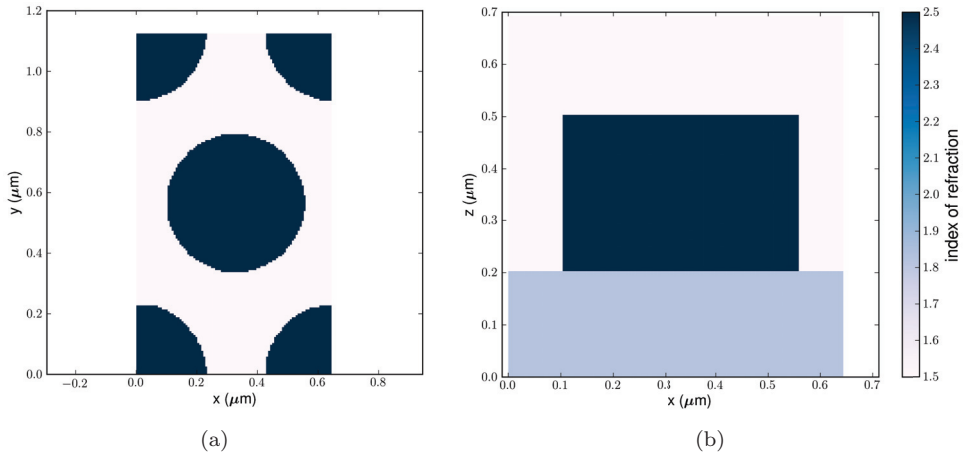


Fig. 12. x - y (a) and x - z (b) cross-section of a PhC design of triangular placed poles. The x - y section is at a height (z) of $0.3 \mu\text{m}$ and the x - z section is taken at a $y = 0.652 \mu\text{m}$. The index of refraction is 1.82 for the scintillator, 2.5 for the PhC and 1.5 for the glue.

3.4.1. The influence of period and feature width

In the following two plots, the influence of a PhC period (L) and feature width (D) change can be seen. The feature width, in this case the pole diameter, is given as a fraction of L . In Fig. 13 the light extraction gain is calculated for an isotropic input function and in Fig. 14 it is calculated for a Teflon wrapped $2 \times 2 \times 15 \text{ mm}^3$ LYSO crystal. It can be seen that the extraction efficiency changes for these two cases which is obvious when considering the difference in AD of a real LYSO pixel a uniform AD.

3.4.2. Index of refraction and absorption

The index of refraction of the PhC material is one of the main factors governing the extraction efficiency. The index of refraction is usually a real number. If one wants

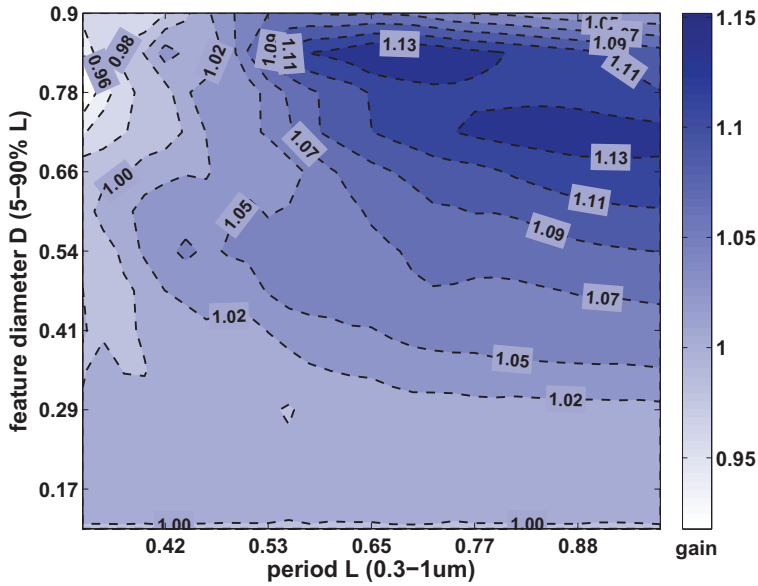


Fig. 13. Gain calculated for an isotropic emitter over different period (L) and feature width (D) values. The impinging light is assumed to have the same power over all impinging angles and is uniformly polarized. The maximum gain was calculated as 1.15 at a period of 675 nm and a 472 nm (70%) pole diameter.

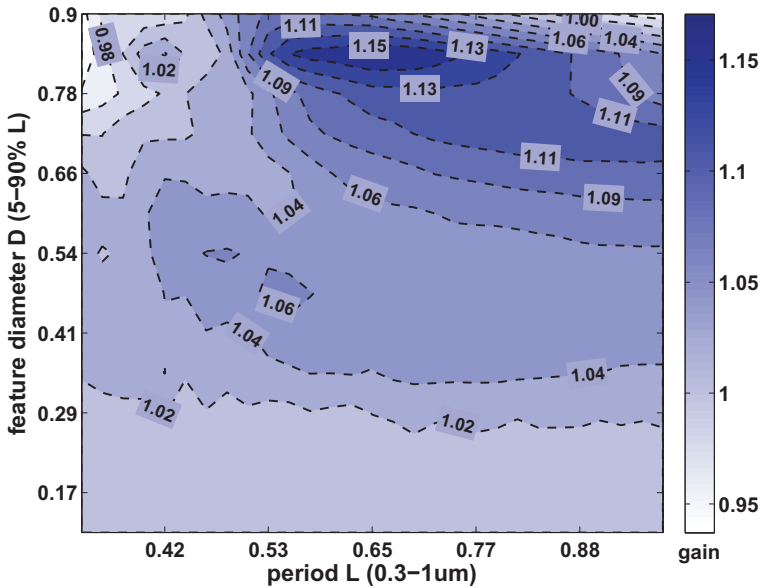


Fig. 14. Gain calculated over different period (L) and feature width (D) values. The impinging light is assumed to come from a Teflon wrapped $2 \times 2 \times 15$ mm³ LYSO crystal. The maximum gain was calculated as 1.17 at a period of 650 nm and a 70% (455 nm) pole diameter.

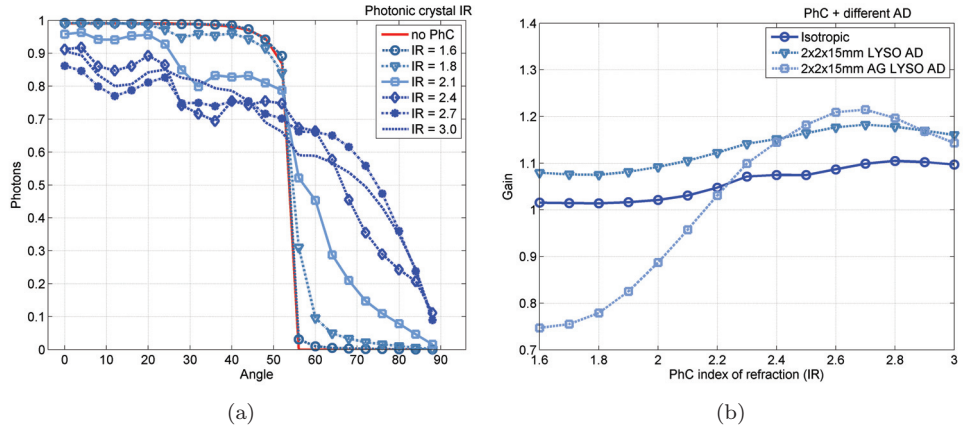


Fig. 15. Influence of the PhC structure index of refraction to the extraction efficiency. Figure (a) shows the extraction probability for each angle and for different index of refractions of the PhC material. Figure (b) shows the light extraction gain cumulated over all possible angles for three different cases of light sources: (1) Isotropic emitter, (2) $2 \times 2 \times 15$ mm LYSO wrapped tightly in Teflon, or (3) a $2 \times 2 \times 15$ mm LYSO wrapped in Teflon but with an air-gap (AG) between crystal and wrapping.

to include the materials absorption in it you just have to give it an imaginary part (k). In our examples we assumed values in the range of real dielectric thin films (e.g. Si_3N_4 , ITO, GaN or TiO_2). The different extraction efficiencies for a changing real part of the IR can be seen in Fig. 15 and the effect of increasing absorption can be seen in Fig. 16.

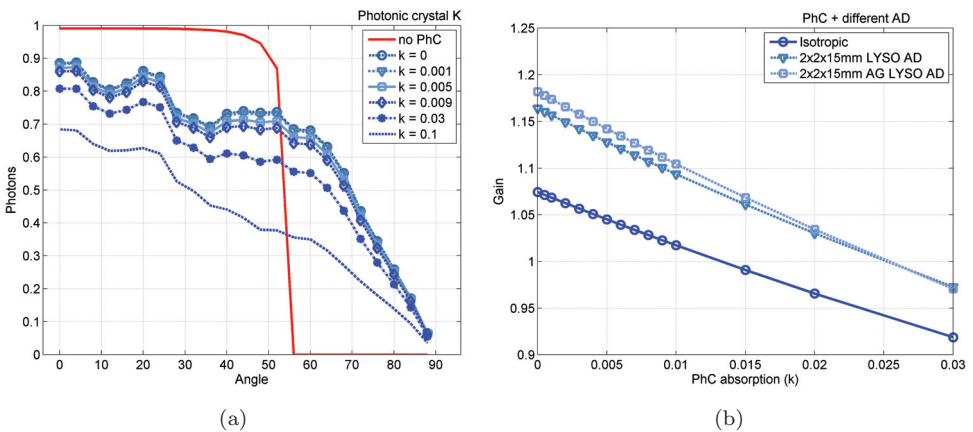


Fig. 16. The light adsorption (k) of the PhC material and its effect on the light extraction efficiency. Figure (b) shows the change of the cumulated gain in respect to the structure adsorption for each of the three crystal configurations.

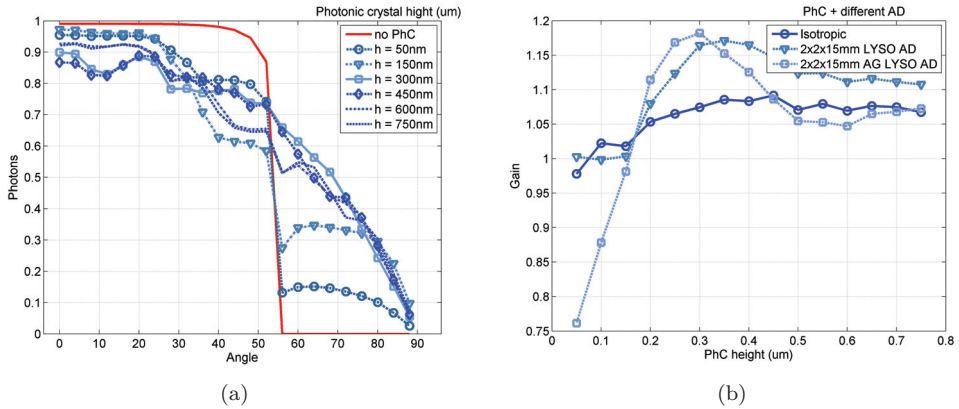


Fig. 17. The PhC structure height and its effect on the extraction efficiency. Figure (b) shows the change of the cumulated gain in respect to the structure height for each of the three crystal configurations.

3.4.3. Structure height

The influence of the structure height can be seen in Fig. 17. An optimum is reached between 300–350 nm. Though one has to say, that in these examples, all the other PhC parameters (e.g. L and D) did not change like in the plots before. If you also adapt period (L) and feature width (D), a similar gain can be achieved in a much broader range of heights (300–500 nm). Nevertheless, a smaller structure height is favorable in the production process. Especially for the masking and reactive ion etching (RIE) steps a structure height larger than 300 nm is bringing additional complications.

3.4.4. Wavelength

The wavelength dependency of the structure is investigated (see Fig. 18) since the LYSO crystal emits light in a broad range of wavelengths. The peak emission of LYSO is at 420 nm but the spectrum contains also photons between 380 nm and 500 nm.

4. Sample Production and Results

The production of a PhC structure on top of a scintillating crystal is a nontrivial procedure. Therefore we have been cooperating with the Lyon Institute of Nanotechnology (INL) which provided valuable knowledge, hands on experience and the right lab equipment for such an approach. For the PhC scintillator sample the standard nanolithography procedure (usually optimized for silicon wafers) using electron beam lithography (EBL) was adapted to the special requirements of our base material. The whole process can be split up in four main parts: Sputtering, Resist spinning, EBL and RIE. The main four lithography steps used for our sample

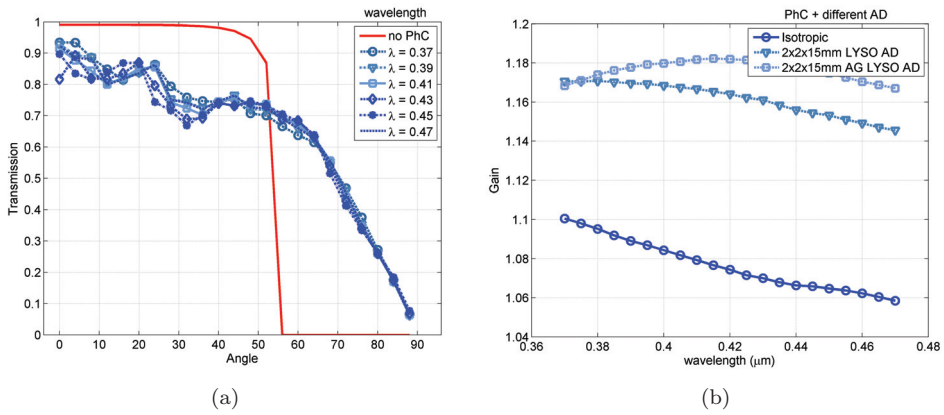


Fig. 18. The photon wavelength and its effect on the extraction efficiency. Figure (b) shows the change of the cumulated gain in respect to the wavelength for each of the three crystal configurations.

are explained in more detail. At the end of the section, the results of the latest PhC samples are shown.

Step 1. Sputter deposition

Since the scintillator is not etched directly, an auxiliary layer of silicon nitrate (Si_3N_4) is applied in the first step by sputter deposition. Sputter deposition is one of several methods of physical vapor deposition (PVD). It is widely used in the semiconductor industry to deposit thin films of various materials. The silicon nitride is used later on as a transfer material for the actual PhC pattern since the scintillator itself cannot be etched by standard nanoetching techniques. The Si_3N_4 is transparent in the emission wavelength of the scintillator and has an index of refraction between 1.8 and 2.0 at 420 nm (Depending on the deposition quality). In addition, an indium tin oxide (ITO) layer is sputtered in between for improving the electrical properties of the sample since ITO is a good electrical conductor and is optically transparent. Other PhC materials with even higher index of refraction can be applied in this step as well and are currently under investigation.

Step 2. Spin coating

Covering the substrate with an electron beam sensitive material is usually the first step after the sample cleaning. The electron beam resist has to be a high-molecular weight polymer dissolved in organic solvents. In our case we were using NANO 950 PMMA A4^b which is a 4% PMMA resist dissolved in Anisol. The aim in the coating step is to get a thin, uniform and defect free polymer film on top of the substrate. An essential parameter is the tone which describes whether the

^bMicroChem Corp., e-beam resist, A4 PMMA.

exposed part or the nonexposed part of the resist becomes soluble in the photoresist developer (positive = exposed parts gets removed, e.g. PMMA). The clearing dose D_{cl} is defined as the amount of charge per unit of area (usually $\mu C/cm^2$) which is necessary to completely develop a large area (area larger than the range of the proximity effects). In addition a high resist contrast is desired, which describes the ratio between the minimal dose D_0 which starts having an effect on the resist to the dose which is necessary to remove 100% of the resist D_{100} . A higher resist contrast would therefore mean better vertical resist profiles.

Resist spinning

The seemingly simple procedure can be quite tricky due to strict requirements toward uniformity and thickness and some unexpected resist behavior. One of the unwanted effects in spinning is caused by the surface tension between resist and air which is leading to boarder effects called “edge beads” (see the thesis of Knapitsch for details).¹² The surface tension at the edge is an additional force directed inwards adding to the viscous force and therefore stops the flow of the resist.³⁶ This edge bed can cover 1–2 mm of the surface from the edge inwards. The thickness can be 10–30 times bigger than the rest of the resist. If the wafer is 10 cm in diameter, this is not considered a big problem since it is just a small fraction of the overall surface. In our case, the edge bead effect has prevented us from using small crystal samples (surfaces smaller than 2 mm in \varnothing) because there the edge effect became predominant over most part of the surface. As a result, we were using bigger crystal samples (10 × 10 mm surface area) where the border regions were skipped in the lithography.

Step 3. Electron beam lithography

The optical resolution requirements of our PhC structure were demanding a highly accurate lithography technique. Since our PhC design contains features as small as 200 nm and requires a minimum tolerance of 10% to make it work efficiently, it comes down to a lithography method that can resolve at least 20 nm structures. We were also interested in fast prototyping of single pieces of a few different PhC designs which is enough to our concept in the first stage. The goal of the EBL is the patterning of a polymer based resist layer with an electron beam. The serial process exposes a single area at a time; this has the disadvantage of being limited in the overall size of the pattern but brings flexibility in the pattern design. Depending on the whole system configuration, feature sizes down to 10 nm can be achieved. The limiting factor for the resolution here is not the diffraction of the electron beam but the forward- and back-scattering of the electrons in the resist and the substrate. For small scale EBL production it is common to use a standard electron beam microscope with some additional hardware and software to keep the costs down. After the e -beam exposure, the sample is developed using a chemical developing

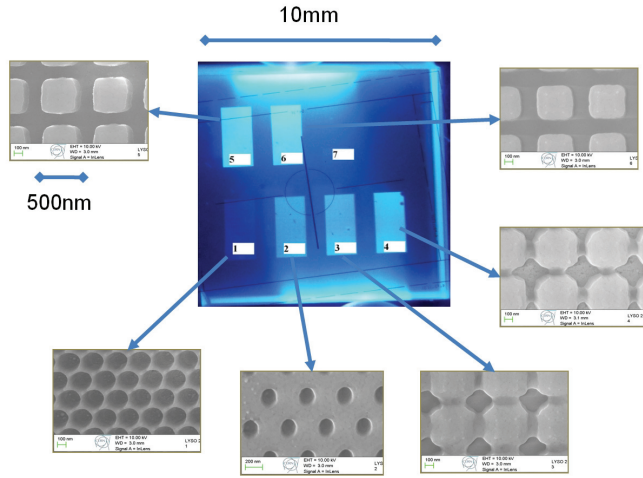


Fig. 19. Scanning electron pictures of the six different PhC patterns produced on top of the $10 \times 10 \times 5$ mm large base LSO crystal.

agent which washes out the exposed areas of the PhC pattern and therefore showing the underlying substrate in these regions.

Step 4. Reactive ion etching

The pattern itself has to be etched using RIE. RIE uses fluorine-containing chemically reactive plasma to transfer the PhC pattern from the PMMA resist into the Si_3N_4 . The plasma is generated in a vacuum chamber by an electromagnetic field and a mixture of different reactive gases. In particular, the alternating electric field caused by a RF generator is stripping of the electrons of the gas. Due to their lower mass, electrons are much more deflected by the oscillating field than the heavier positive ions and are therefore more likely to be absorbed by the surrounding chamber or target. Because the chamber is grounded, the bottom plate is DC isolated and therefore builds up a negative charge. Since the positive ions from the plasma are moving in the direction of the negative bottom plate, an anisotropic etch profile can be created at the target. The anisotropic etching ensures a constant hole diameter from the top to the bottom of the PhC slab, in contrast to the typical isotropic profiles of wet chemical etching. The control of the etching rate is related to many parameters, the most important are the chamber pressure, the gas flow, and the RF power.

4.1. Results

Six different PhC patterns were produced on top of a $10 \times 10 \times 5$ mm LSO:Ce scintillator (see scanning electron microscope (SEM) picture in Fig. 19). The PhC material was chosen to be silicon nitrate (Si_3N_4) and the pixels were cut out after the lithography (see Fig. 20).

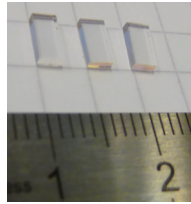


Fig. 20. Cut and polished pixels of LSO covered with a PhC silicon nitride structure.

Because of an uncertainty of $\pm 30\%$ in the resist thickness of the actual sample, the dose-factor for the e -beam process could not be determined exactly. This uncertainty can lead to over- or under-exposure of the resist and a deviation of the pattern as a consequence. Due to this fact, we exposed several patterns with different dose-factors so that we could experimentally figure out the right dose after the lithography. The SEM pictures showed the best agreement on pattern Nr. p6 (right picture in Fig. 21). On pattern p3 (left picture in Fig. 21) we can see the same pattern when underexposed. Also on pattern p1 and p2 we can see deformations which can be related to over- and under-exposure.

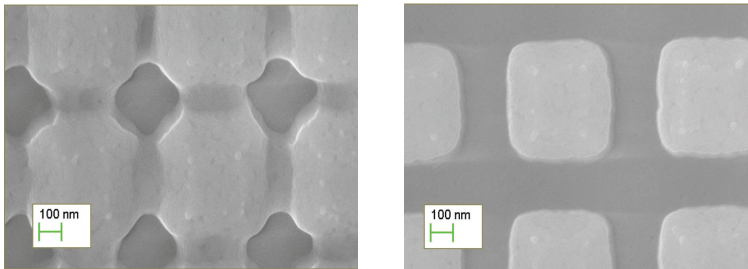


Fig. 21. Scanning electron microscope pictures of the square pillar structure etched into the silicon nitride layer on top of the scintillator. The pattern is of the same design (design parameters: $a = 640$ nm, $d = 500$ nm) but with different dose factors. In pattern p3 (left) one can see the effect of underexposure whereas the dose factor for p6 (right) leads to the closest match to the pattern designs.

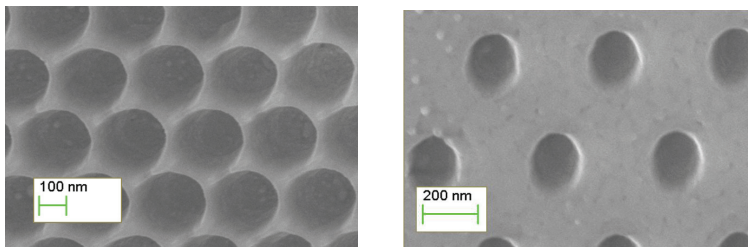


Fig. 22. Scanning electron microscope pictures of the triangular placed PhC structure etched into the silicon nitride layer on top of the scintillator. In pattern p1 (left, design parameters: $a = 280$ nm, $d = 170$ nm) we have severe over-exposure. On pattern p2 (design parameters: $a = 450$ nm, $d = 220$ nm) we have under-exposure.

4.1.1. Light extraction gain

The lithography was performed on a $10 \times 10 \times 5$ mm LYSO scintillator (see SEM picture in Fig. 19). Four different patterns survived the cutting and polishing procedure which was necessary to get single scintillator pixels. These four PhC patterns can be seen in Figs. 21 and 22. To see the light extraction gain on the PhC modified scintillator pixels, two different measurements were performed. The results were then compared to a reference sample which was cut from the same LYSO crystal and also has undergone the same treatment in the whole lithography procedures but is without any patterns. We have shown that nanostructuring a layer of higher index of refraction than Si_3N_4 would allow reaching similar improvement factors as compared to the standard configuration of a plane surface optically coupled to the photodetector with a glue or optical grease.

Angular distribution and light collimation

The scintillator was excited with a UV light source in order to generate a satisfyingly bright signal. The extracted light was measured by a photodiode mounted on a goniometer centered in the middle of the PhC. The measurement results can be seen in the polar angular plots of Fig. 23. It can be seen that all of the PhC scintillators are showing a stronger signal than the unpatterned reference crystal.

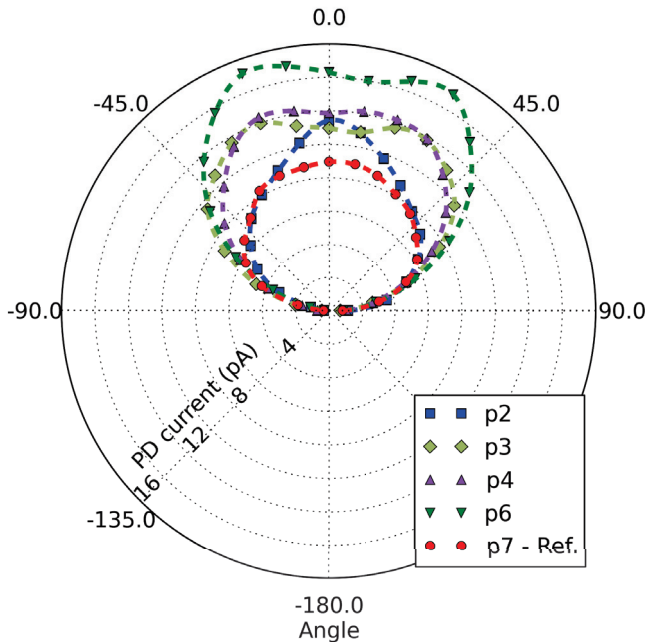


Fig. 23. Polar angular plot of the measured light emission from the different PhC scintillator samples compared with an unstructured reference sample (p7).

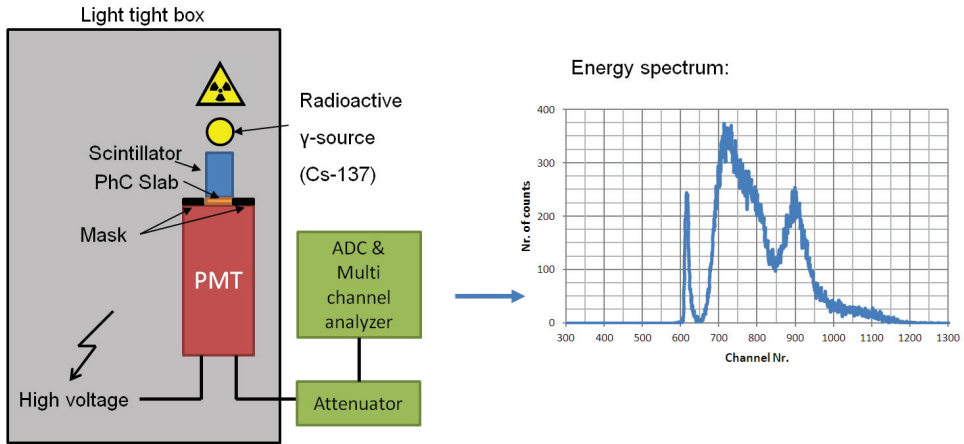


Fig. 24. Light yield measurement setup. The light yield of the samples was measured using photons of 662 keV coming from a Cs137 source. The crystals are placed on top of a XP2262 PMT with and without optical glue and wrapping. The PMT window has been masked to measure only the light coming from the PhC surface of the scintillator.

In addition a slightly different radiation pattern can be observed from each of the PhC samples. Especially interesting is the light collimation effect observed on p2. Even though it does not have the strongest light yield gain, this effect could be further optimized and exploited for applications where a strong focusing of the emitted light is desired. As an example, the light collimation could be interesting in devices which have some distance between scintillator and photo detector or if one wants to couple the scintillation light to a light guiding fiber which does not cover the whole scintillator extraction surface.

Light yield gain

For the light yield, the samples were measured using a photomultiplier tube (PMT) and a Cs137 source (662 keV gamma rays) for excitation. A mask was prepared such that only the light coming from the PhC area was taken into account for the measurements. The whole setup was temperature stabilized at 20°C. Figure 24 shows the schematics of the setup. Six different PhC structures were prepared on top of the LSO crystal (see Fig. 19). Pattern Nos. 1 and 5 did not survive the cutting and polishing process, which left us four different PhC structured scintillators with the dimensions of $1.2 \times 2.6 \times 5 \text{ mm}^3$. In addition, a reference crystal was cut from the same base crystal, which has been treated as the same way then the PhC samples just without a pattern (including the ITO and silicon nitride layer, see area No. 7 in Fig. 19). After cutting they have been polished on all side walls. The crystals were measured without optical glue and without Teflon wrapping. In Table 5 the light yield and the light yield gain relative to the reference crystal is shown. For completeness, the samples have been measured

Table 5. Mean values of the light yield [Pht/MeV] of the different PhC samples measured without wrapping and without optical glue. The gain is calculated as a ratio between the light yield of the PhC crystal and the reference crystal p7-ref. The measurement uncertainty in the setup was specified as $\pm 7\%$ and the standard deviation of the measurements is below that uncertainty.

	p7-ref	p2	p3	p4	p6
LY [Pht/MeV]	2168	2279	2841	2815	3383
Gain	1.00	1.05	1.31	1.30	1.56

Table 6. Light yield gain relative to the reference crystal of the four different PhC sample crystals. The crystals were measured in four different states: without wrapping and optical glue, with optical glue only, with Teflon wrapping only, and finally with Teflon wrapping and optical glue.

	p2	p3	p4	p6
Air	1.05	1.31	1.30	1.56
Glue	0.70	0.85	0.74	0.69
Teflon	1.17	1.05	0.94	1.28
Glue + Teflon	0.96	0.93	0.92	0.99

with optical glue, with Teflon wrapping and with glue and Teflon wrapping. Since the PhC was optimized to diffract best into air as an out coupling medium, it shows lower light output when using glue.

5. Mass-Production Technologies

Electron beam lithography (EBL) is the preferred lithography technique in prototyping. It is a cheap technique and provides flexibility in the pattern design. The disadvantage is the limited throughput. Due to the scanning nature of the technique, the overall size of the sample is limited by the lithography time. For our sample the EBL took approximately 30 min for each mm^2 and we already tried to speed up the process by using high e -beam currents and small beam settling times which has the downside of decreasing the pattern quality. In addition, just one sample per run can be treated. If one looks now for possibilities of a large area and high throughput production, one has to consider for different lithography techniques. In industry, there are two different ways to cope with that problem, optical interference lithography (IL) and nanoimprint lithography (NIL).

5.1. Optical interference lithography

Optical Interference Lithography (IL) is a holographic approach where two or more coherent beams interfere to produce a standing wave in the form of the desired pattern.³⁷ The interference pattern should look like the desired pattern or the negative of it (depends if one uses a positive or negative photo-resist). The exposed areas

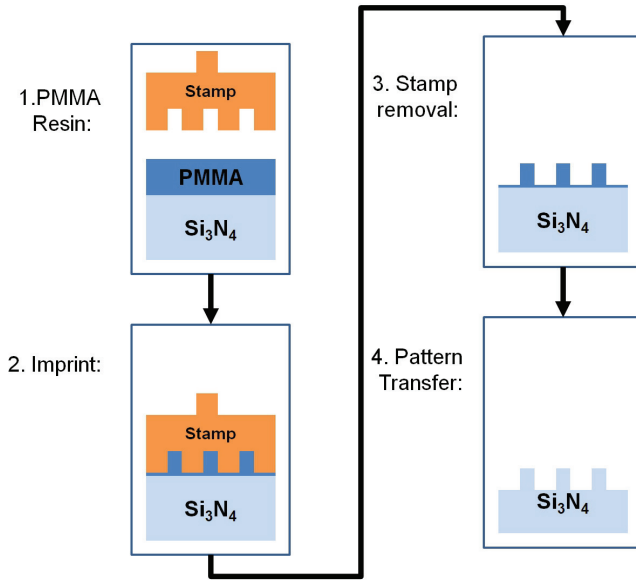


Fig. 25. The different NIL steps. A premanufactured stamp containing the negative of the pattern is imprinted on a PMMA resin which results in the mask for the pattern transfer in the last step.

are developed and etched like in most other lithography methods. The restriction for that technique is that the pattern has to be periodic in a way that can be re-assembled by the superposition of plane waves. The advantage of optical IL is the large area which can be exposed within a short time.

5.2. Nanoimprint lithography

The nanoimprint lithography (NIL) technique combines the high throughput of a “mask-based” lithography approach with the accuracy and resolution of a low-throughput method like EBL. In the patterning process, a stamp (mold) containing the negative of the desired pattern which was previously manufactured using highly accurate but low throughput approaches is used to mechanically stamp a resist material (see Fig. 25).³⁸ The pattern in the resist can then be transferred using standard pattern transfer methods like RIE.

6. Conclusion

The potential of PhCs to increase the light extraction efficiency of HISs has been demonstrated by the authors and confirmed by others in subsequent studies. In this review paper the theoretical background of this performance gain has been outlined in detail. We describe in particular the complete and versatile simulation framework we have developed, combining a light ray-tracing program for the scintillator and a coupled wave analysis software package for the simulation of the

optics in PhCs. In general, the simulation predicts a substantial light extraction improvement for various scintillator materials and pixel shapes based on the special light diffraction properties of PhC layers. Moreover we also showed the influence of changing PhC designs on the expected light extraction gain at different impinging angles. The production routines of our PhC prototypes have been outlined including the optimization of the different steps of the fabrication techniques, particularly the deposition of the layer to be nanostructured, the spin-coating of the PMMA resin and the RIE for the pattern transfer. Based on the gained experience in the EBL samples, methods for a mass production technology are proposed. The results of a proof-of-principle test with six different PhC patterns deposited on a small $10 \times 10 \times 5$ mm LSO crystal confirm a significant gain in the light extraction efficiency, reaching in the best case a factor 1.56 for extraction in air. This increase in light output has a direct impact on the timing resolution of the scintillator by improving the photo-statistics. Moreover a redistribution of the light propagation modes and a reduction of the light bouncing in the crystal are expected to further improve the timing resolution in long crystals. As this first experiment was made on a short crystal (5 mm) this improvement was not likely to be significant but the observed modification of the AD of the emitted photons confirms the hypothesis of the influence of the PhCs on the light propagation modes.

Acknowledgments

Many thanks to Dominique Deyrail (CERN, PH/CMX) for cutting and polishing the LSO/LYSO samples. Thanks as well to the staff of the INL (Institut des Nanotechnologies de Lyon-INL) which helped me producing the PhC structures in their laboratories.

References

1. P. Lecoq, E. Auffray, S. Brunner, H. Hillemanns, P. Jarron, A. Knapitsch, T. Meyer and F. Powolny, *IEEE Trans. Nucl. Sci.* **57**, 2411 (2010).
2. M. Kronberger, E. Auffray and P. Lecoq, *IEEE Trans. Nucl. Sci.* **55**, 1102 (2008).
3. S. Gundacker, Time resolution in scintillator based detectors for positron emission tomography, Ph.D. thesis, Vienna University of Technology (2014).
4. E. Yablonovitch, *Phys. Rev. Lett.* **58**, 2059 (1987).
5. S. John, *Phys. Rev. Lett.* **58**, 2486 (1987).
6. E. Yablonovitch and T. J. Gmitter, *Phys. Rev. Lett.* **63**, 1950 (1989).
7. R. K. Lee, Y. Xu and A. Yariv, *J. Opt. Soc. Am. B* **17**, 1438 (2000).
8. J. J. Wierer, M. R. Krames, J. E. Epler, N. F. Gardner, M. G. Craford, J. R. Wendt, J. A. Simmons and M. M. Sigalas, *Appl. Phys. Lett.* **84**, 3885 (2004).
9. A. David, C. Meier, R. Sharma, F. S. Diana, S. P. DenBaars, E. Hu, S. Nakamura, C. Weisbuch and H. Benisty, *Appl. Phys. Lett.* **87**, 101107 (2005).
10. A. Knapitsch, E. Auffray, C. W. Fabjan, J.-L. Leclercq, P. Lecoq, X. Letartre and C. Seassal, *Nucl. Instrum. Methods Phys. Res. A* **628**, 385 (2011).
11. A. Knapitsch, E. Auffray, C. W. Fabjan, J.-L. Leclercq, X. Letartre, R. Mazurczyk and P. Lecoq, *IEEE Trans. Nucl. Sci.* **59**, 2334, 2339 (2012), doi: 10.1109/TNS.2012.2184556.

12. A. R. Knapitsch, Photonic crystals: Enhancing the light output of scintillation based detectors, Ph.D. thesis, Vienna University of Technology (2012).
13. P. Pignalosa, B. Liu, H. Chen, H. Smith and Y. Yi, *Opt. Lett.* **37**, 2808 (2012).
14. Z. Zhu, B. Liu, C. Cheng, Y. Yi, W. Guo, S. Huang, H. Chen, M. Gu, C. Ni and X. Liu, *Opt. Mater.* **35**, 2343 (2013).
15. Z. Zhu, B. Liu, C. Cheng, H. Chen, M. Gu, Y. Yi and R. Mao, *Phys. Status Solidi A* **211**, 1583 (2014).
16. J. Cates, J. Hayward and X. Zhang, *IEEE Trans. Nucl. Sci.* **60**, 1027 (2013).
17. L. Biró, K. Kertész, Z. Vértesy, G. Márk, Z. Bálint, V. Lousse and J.-P. Vigneron, *Mater. Sci. Eng. C* **27**, 941 (2007) [EMRS 2006 Symposium A: Current trends in nanoscience — From materials to applications].
18. H. Ibach and H. Lüth, *Solid State Physics: An Introduction to Principles of Materials Science*, Advanced Texts in Physics (Springer, 2003).
19. S. G. Johnson and J. D. Joannopoulos, *Opt. Express* **8**, 173 (2001).
20. S. G. Johnson, S. Fan, P. R. Villeneuve, J. D. Joannopoulos and L. A. Kolodziejski, *Phys. Rev. B* **60**, 5751 (1999).
21. R. Hagen, Spectral investigation of a 2-dimensional photonic crystal slab for mid-infrared radiation, Ph.D. thesis, University of Twente (2007).
22. P. Lecoq, E. Auffray, S. Gundacker, H. Hillemanns, P. Jarron, A. Knapitsch, J. Leclercq, X. Letartre, T. Meyer, K. Pauwels, F. Powolny and C. Seassal, Progress on photonic crystals, in *Nuclear Science Symposium Conference Record (NSS/MIC)*, 30 Oct.–6 Nov. 2010, pp. 1970–1975.
23. A. A. Erchak, D. J. Ripin, S. Fan, P. Rakich, J. D. Joannopoulos, E. P. Ippen, G. S. Petrich and L. A. Kolodziejski, *Appl. Phys. Lett.* **78**, 563 (2001).
24. J. D. Joannopoulos, S. G. Johnson, J. N. Winn and R. D. Meade, *Photonic Crystals: Molding the Flow of Light*, 2nd edn. (Princeton University Press, 2008).
25. J. J. Wierer, A. David and M. M. Megens, *Nat. Photon.* **3**, 163 (2009).
26. A. David, H. Benisty and C. Weisbuch, *Disp. Technol. J.* **3**, 133 (2007).
27. F.-X. Gentit, *Nucl. Instrum. Methods Phys. Res. A* **486**, 35 (2002) [Proceedings of the 6th International Conference on Inorganic Scintillators and their Use in Scientific and Industrial Applications].
28. R. Brun and F. Rademakers, *Nucl. Instrum. Methods Phys. Res. A* **389**, 81 (1997) [New Computing Techniques in Physics Research V].
29. P. Beckmann and A. Spizzichino, *The Scattering of Electromagnetic Waves from Rough Surfaces* (Pergamon Press, New York, 1963).
30. J. E. Harvey, A. Krywonos and C. L. Vernold, *Opt. Eng.* **46**, 078002 (2007).
31. G. Guohua, K. Songfeng, S. Xiubao and C. Qian, *Opt. Quantum Electron.* **41**, 453 (2009), doi: 10.1007/s11082-010-9378-y.
32. C. G. Bostan, Design and fabrication of quasi-2d photonic crystal components based on silicon-on-insulator technology, Ph.D. thesis, University of Twente, Enschede (2005).
33. P. Bienstman, Rigorous and efficient modelling of wavelength scale photonic components, Ph.D. thesis, Universiteit Gent (2001).
34. J.-P. Berenger, *J. Comput. Phys.* **114**, 185 (1994).
35. M. G. Moharam and T. K. Gaylord, *J. Opt. Soc. Am.* **71**, 811 (1981).
36. H. Levinson, *Principles of Lithography*, Press Monographs (SPIE Press, 2005).
37. M. Maldovan and E. L. Thomas, *Periodic Materials and Interference Lithography for Photonics, Phononics and Mechanics*, 1st edn. (Wiley-VCH, 2008).
38. S. Y. Chou, P. R. Krauss and P. J. Renstrom, *J. Vac. Sci. Technol.* **14**, 4129 (1996).